⌘ *Author's Choice*

THE JOURNAL OF BIOLOGICAL CHEMISTRY VOL. 287, NO. 9, pp. 6904–6911, February 24, 2012

In Channelrhodopsin-2 Glu-90 Is Crucial for Ion Selectivity and Is Deprotonated during the Photocycle*[S]

Received for publication, November 28, 2011, and in revised form, December 30, 2011 Published, JBC Papers in Press, January 4, 2012, DOI 10.1074/jbc.M111.327700

Kirstin Eisenhauer[‡1], Jens Kuhne[‡1], Eglof Ritter[§], André Berndt[¶2], Steffen Wolf[‖3], Erik Freier[‡], Franz Bartl[§], Peter Hegemann[¶], and Klaus Gerwert[‡‖4]

From the [‡]Department of Biophysics, Ruhr-University Bochum, Universitätsstrasse 150, Bochum 44801, Germany, the [§]Institut für medizinische Physik und Biophysik, Charité, Universitätsmedizin Berlin, Charitéplatz 1, Berlin 10117, Germany, the [¶]Institut für Biologie, Experimentelle Biophysik, Humboldt-Universität zu Berlin, Invalidenstrasse 42, Berlin 10115, Germany, and the [‖]CAS–Max-Planck Partner Institute for Computational Biology, Shanghai Institutes for Biological Sciences, 320 Yue Yang Road, Shanghai 200031, China

Background: Channelrhodopsin-2 is a light-gated ion channel extensively used in optogenetics.
Results: Glu-90 is deprotonated in the open state and is crucial for ion selectivity.
Conclusion: Protonation change of Glu-90 is part of the opening/closing of the conductive pore, and the functional protein unit is assumed to be the monomer.
Significance: Understanding the gating mechanism is necessary for optimizing this optogenetic tool.

The light-activated microbial ion channel channelrhodopsin-2 (ChR2) is a powerful tool to study cellular processes with high spatiotemporal resolution in the emerging field of optogenetics. To customize the channel properties for optogenetic experiments, a detailed understanding of its molecular reaction mechanism is essential. Here, Glu-90, a key residue involved in the gating and selectivity mechanism of the ion channel is characterized in detail. The deprotonation of Glu-90 during the photocycle is elucidated by time-resolved FTIR spectroscopy, which seems to be part of the opening mechanism of the conductive pore. Furthermore, Glu-90 is crucial to ion selectivity as also revealed by mutation of this residue combined with voltage clamp experiments. By dynamic homology modeling, we further hypothesized that the conductive pore is flanked by Glu-90 and located between helices A, B, C, and G.

Microbial rhodopsins, particularly the channelrhodopsin family of green algae, have come into the focus of neurobiological research as very useful tools to study connections and the functioning of neuronal networks (optogenetics). The light-activated ion channel channelrhodopsin-2 (ChR2)[5] (1, 2) has become the cornerstone of this emerging field. Like all other known microbial rhodopsins, ChR2 spans the membrane in seven transmembrane helices (7-TM), and the chromophore retinal is covalently attached to a lysine via a protonated Schiff base.

Although a broad variety of optogenetic applications exists (recently reviewed in Ref. 3), only the general three-dimensional structure of the 7-TM protein domain is known from electron microscopy studies (4); the amino acid arrangement, the location of the ion pore, and the molecular mechanism of pore opening (gating) and charge transfer remain unknown.

On the other hand, extensive electro-physiological and spectroscopic studies in the visible and infrared regions have been performed on ChR2, revealing the kinetics of the gating process, photocycle intermediates, and structural changes of the protein, irrespective of where these changes occur. Light excitation triggers, as in all other microbial rhodopsins, a cyclic sequence of reactions initiated by an ultrafast all-*trans* to 13-*cis* retinal isomerization (5). After the formation of two early photoproducts, P500 and P390 (6, 7), the conducting state P520 is reached within 1.5 ms after photon absorption (on-gating) and disappears within 10 ms (off-gating). The protein then returns to the fully dark-adapted state via the late P480 intermediate within a few seconds (6–8). Light activation is accompanied by large structural changes that occur during P500 formation. These changes clearly precede pore opening and are reversed during the decay of the late intermediate, P480, which is not concomitant with channel closing (7, 9). Deprotonation and reprotonation of the RSB-H^+ are observed as the formation and decay of the blue-shifted P390 intermediate in the ChR2 photocycle. Reprotonation correlates with channel on-gating (6, 7) but not with the large structural changes. However, we can draw similarities between the molecular mechanisms of the well studied microbial rhodopsin proton pump bacteriorhodopsin (BR) (10) and those of ChR2, in the sense that isomerization, protonation changes of the Schiff base and internal Asp/Glu, and motions of protein-bound water molecules are likely to be key elements of channel gating as well as of proton

* This work was supported by the Deutsche Forschungsgemeinschaft (Grants HE3824/9-1 and 17-1 to P. H. and BA 2242/ 2-1 to F. B.).
⌘ *Author's Choice*—Final version full access.
[S] This article contains supplemental Figs. S1–S6, text, and references.
[1] Both authors contributed equally to this work.
[2] Supported by the Leibniz Graduate School for Molecular Biophysics.
[3] Funded by a Chinese Academy of Sciences Fellowship for Young International Scientists.
[4] Acknowledges a fellowship from the Mercator Foundation. To whom correspondence should be addressed: Dept. of Biophysics, Ruhr-University Bochum, Universitätsstrasse 150, Bochum 44801, Germany. Tel.: 49-234-32-24461; E-mail: gerwert@bph.rub.de.
[5] The abbreviations used are: ChR1/2, Channelrhodopsin-1/2; 7-TM, 7-transmembrane; BR, bacteriorhodopsin; I_0, initial current; I_S, stationary current; VChR1/2, *Volvox cateri* channelrhodopsin-1/2; MD, molecular dynamics; PC, phosphatidylcholine; BTP, 1,3-bis-[tris(hydroxymethyl)methylamino]-propane pH_o, pH out; pH_c, pH cytoplasmic; RSB, retinal Schiff Base.

and cation transport. From spectroscopic as well as electrophysiological studies we know that the same residue positions that are important for BR function are also important for channel gating, ion-transport, ion selectivity, and rectification of the ChR2 channel. Recently, several research groups have shown that His-134 (Asp-96 in BR), together with Glu-90 (BR analog not yet resolved), forms the major selectivity filter (11–13). Residues at this position determine the conductance of H^+ and Na^+ as well as the competition between the two ions (11–14). Moreover, mutations in Glu-123 (Asp-85 in BR), which is thought to form the RSB-H^+ counterion complex together with Asp-253 (Asp-212 in BR), cause variable shifts of the action spectrum, acceleration of photocycle kinetics, and alterations in the voltage dependence of the gating current (15–17). Mutations in Cys-128 and/or Asp-156, the ChR2 residues equivalent to those in BR forming the important link between helices C and D (Thr-90 and Asp-115 (18)), cause a dramatic slowdown of the photocycle and result in extended depolarization of cells after a single light flash (step function rhodopsins) (3, 8, 19, 20).

However, the major difference between ChR2 and BR is in the ion pore. The pore must be larger in ChR2 to conduct cations and must be continuous across the membrane to passively conduct multiple ions per photocycle. On the other hand, in BR, the pore is small and discontinuous during the whole photocycle to allow only the transport of protons and to prevent spontaneous backflow along the proton gradient across the membrane (21, 22). Although recent studies revealed projection maps of ChR2 two-dimensional crystals at ~6-Å resolution, the localization of the conductive pore in ChR2 remains unclear (4). Based on these projection maps, two different positions of the conductive pore in ChR2 are possible: either within the monomeric protein or within the dimeric interface (4). Therefore, identification of the enlarged pore in ChR2 and the unraveling of its opening mechanism with high spatial and temporal resolution comprise the key requirement for further optimization of this optogenetic tool.

Time-resolved Fourier transform infrared (FTIR) spectroscopy in combination with structural details can provide insights into the molecular reaction mechanism. Due to the absence of an x-ray structure, homology modeling incorporating experimental constraints is a valuable technique to provide a structural model, which can inspire further experiments (22–25). Based on electrical studies on Glu-90 mutants and changes in hydrogen bonding during the photocycle, this position is believed to be crucial for the conductance and selectivity of the channel (7, 12–14). We determined the protonation of and environmental changes around Glu-90 by time-resolved FTIR spectroscopy. This method was one of the major techniques used in elucidating the ion transfer mechanism in BR (26–28). To characterize the role of Glu-90 for the conductive behavior of ChR2, we performed electro-physiological measurements. We then built a dynamic homology model (29) for ChR2 based on the BR x-ray structure 1QHJ (30) to assess the structural influence of a protonation change at Glu-90. This method has successfully been employed to gain insight into the proton transfer mechanism of BR (21, 22) as well as in studying ligand recognition and discrimination in G protein-coupled receptor (25, 31). Based on the orchestration of biophysical experiments and biomolecular simulations, we have localized the pore of ChR2 between helices A, B, C, and G and identified protonation changes of the key residue Glu-90 as being an essential part of the pore function.

EXPERIMENTAL PROCEDURES

Expression, Purification, and Lipid Reconstitution of Channelrhodopsin-2—Channelrhodopsin and its mutants were expressed in COS-1 cells as described previously (32). Synthetic ChR-2 DNA fragments comprising amino acids 1–311 of the protein with a C-terminal 1D4 epitope (33) were used. Site-directed mutagenesis, reconstitution with the chromophore, and purification of the protein were performed as described earlier for bovine rhodopsin (34–36), with the following modifications: 30 mM all-*trans*-retinal (Sigma) was used for reconstitution, and the last step of the elution was performed in a buffer containing the detergent *n*-D-octyl-β-D-glycopyranoside. For reconstitution of the proteins into lipid vesicles, Egg-PC (Avanti Polar Lipids, Inc.) was first lyophilized, suspended in buffer (20 mM BTP, 120 mM NaCl, 1 mM $MgCl_2$), repeatedly frozen in liquid nitrogen, and thawed in tepid water (25 °C) and finally extruded through a 200-nm polycarbonate membrane extruder. The lipid vesicles were then incubated with the purified protein for 2 h and dialyzed for 5 days at 4 °C in the same buffer with the addition of 1 mM dithiothreitol. The lipid:protein ratio was 100:1. All preparation steps were performed under dim red light. Samples for FTIR measurements were prepared by a centrifugation procedure; after adjusting the pH with diluted NaOH or HCl, 20 μl of the sample was centrifuged for 30 min at 100,000 × *g* at 4 °C. The supernatant was then removed, and the pellet was transferred to an air-tight infrared cuvette consisting of two CaF_2 windows.

FTIR Measurements—The sample was then cooled to 15 °C by a homemade sample holder in a Bruker Vertex 80V FTIR spectrometer. To excite the sample to the photostationary state, it was illuminated for ~5 s by 3 light-emitting diodes with an emission maximum of 463 nm. During illumination and relaxation, spectral changes were recorded using the rapid scan mode of the spectrometer. Absorbance spectra were calculated and later analyzed by a global fit method to obtain the amplitude spectra and half-lives of the processes (as done for measurements shown in Fig. 1).

To obtain accurate time courses of the photocycle, we carried out laser flash experiments. The sample was excited by flashes (maximum of 20 ns) of an excimer-pumped dye laser (coumarin 102; 470 nm maximum emission peak). After the flash, we recorded spectral changes using the rapid scan mode (as done for measurements shown in Fig. 2).

UV-visible Measurements—UV-visible measurements were performed under the same conditions as the FTIR measurements, except for the measuring light intensity, which was kept as low as possible to avoid the accumulation of intermediates. To obtain the counterpart of the FTIR results in the visible frequency range, the data were combined with the previously recorded FTIR data and a global fit over the whole spectral range was done.

Homology Modeling and MD Simulations—Dynamic homology modeling of ChR2 was performed as previously described

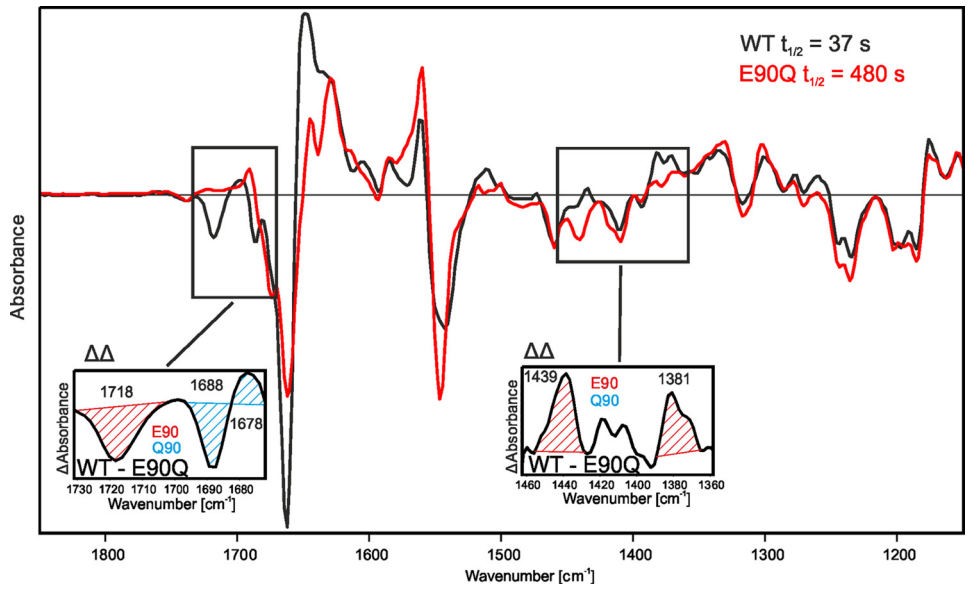

FIGURE 1. **P480 to D470 relaxation rates of ChR2 WT and E90Q.** Amplitude spectra of the relaxation rate from P480 to D470 of WT ChR2 (*black*) and the mutant E90Q (*red*) are shown. The negative carbonyl band of Glu-90 at 1718 cm^{-1} and the corresponding positive carboxylate band, either at 1381 cm^{-1} or 1439 cm^{-1}, are missing in the mutant. The *insets* show the subtraction results of the WT and E90Q spectra. The C=O (1718 cm^{-1}, *red stripes*) of Glu-90 and its corresponding COO$^-$ band (1381 cm^{-1} or 1439 cm^{-1}, *red stripes*) disappear in the mutant. Therefore, these bands can be unambiguously assigned to Glu-90 deprotonation. In Gln-90, which has a fixed protonation state, a difference band at 1688/1678 cm^{-1} (*blue stripes*) is observed, which indicates its H-bond or environmental change.

(29). Briefly, a multiple sequence alignment comprising the sequences of ChR2 (Uni-Prot ID: Q8RUT8), BR (P02945), and nine other microbial rhodopsins (P15647, Q2S2F8, bQ9AFF7, P25964, P42196, Q8YSC4, B4Y105, B4Y103, and A8JAJ2) was used as the starting point. Model building on the basis of the BR ground-state structure with PDB ID 1QHJ (30) was performed using the SCWRL3 algorithm (37) and the MOBY program package (38). Molecular dynamics (MD) simulations in an explicit palmitoyl oleoyl phosphatidyl choline/solvent (39) environment were carried out using GROMACS software v.4.0.5 (40) as described previously (29). Further details can be found in the supplemental material.

Electrophysiology—Voltage clamp experiments on heterologously expressed ChR2 were carried out in *Xenopus* oocytes as described earlier (2, 17). Cytoplasmic free cation concentrations (in mM) were ~2 Mg^{2+}, <0.001 Ca^{2+}, ~110 K^+, ~10 Na^+, pH_c 7.3 in oocytes (R_f), and 110 Na^+, <0.001 Ca^{2+} (10 EGTA, 2 total Ca^{2+}), 5 K^+, 0.2, 2, or 10 Mg^{2+}, pH_c 7.2 in HEK cells. If not mentioned otherwise, the bath for both systems contained (in mM) 100 *N*-methyl-D-glucosamide$^+$ or Na^+, 2 Ca^{2+}, 2 Mg^{2+}, 2 K^+, pH_o 9.0, 7.5, or 6.0 buffered with 10 Tris or Hepes. Anions are irrelevant here, because they are not conducted by ChR2 (2). Photocurrents were typically studied 3–7 days after RNA injection. A 75-watt xenon lamp (Jena Instruments) combined with a fast shutter (Uniblitz model T132, Vincent Associates) was used for light pulses. Blue light was selected with a dichroic mirror reflecting 450–90 nm light through the lens onto the sample. 100% light intensity corresponded to 4.5×10^{21} photons m^{-2} s^{-1} at the cell surface.

RESULTS

FTIR Spectroscopic Results—We applied time-resolved FTIR spectroscopy to determine protonation changes at Glu-90 by comparing WT ChR2 and the E90Q mutant. The IR amplitude spectra of the P480 to D470 relaxation rates of both proteins were in good agreement, allowing band assignment using this mutant (Fig. 1). In the carbonyl region, a negative band at 1718 cm^{-1} was no longer observed in E90Q. Therefore, this disappearing band can be unambiguously assigned to the deprotonation of Glu-90. The corresponding positive carboxylate band is most likely either the one at 1439 cm^{-1} or at 1381 cm^{-1} in the WT protein, because both bands disappear in E90Q. These observations provide strong evidence for deprotonation of Glu-90 during the photocycle. This is further confirmed by an absorbance change of Gln-90 in the mutant; its carbonyl band shifts from 1678 cm^{-1} to 1688 cm^{-1}. This also reflects the environmental change at this residue position that may lead to a deprotonation of Glu-90 in the WT protein. In contrast to earlier FTIR investigations (7), which already proposed a hydrogen bond change at Glu-90, the current measurements were performed on ChR2 reconstituted in lipid vesicles, not in detergent, and in an advanced vacuum spectrometer. All these factors resulted in significant improvement in the signal-to-noise ratio, allowing us to distinguish between an H-bond change and a deprotonation.

To assign the IR absorbance changes, especially the deprotonation of Glu-90, to specific photocycle intermediates, we carried out two consecutive time-resolved measurements in the UV-visible and IR regions to follow absorbance changes in the same sample. In both cases, the photoreaction was initiated by the application of a 20 ns laser flash. A global fit analysis was then performed on the complete dataset. This allowed the unambiguous assignment of absorbance changes measured by IR to their respective intermediates, in agreement with earlier UV-visible measurements (7). *Panels A* and *B* in Fig. 2 show the results of the laser flash-induced UV-visible and FTIR measurements, respectively. The *black curve* in Fig. 2*A* represents a

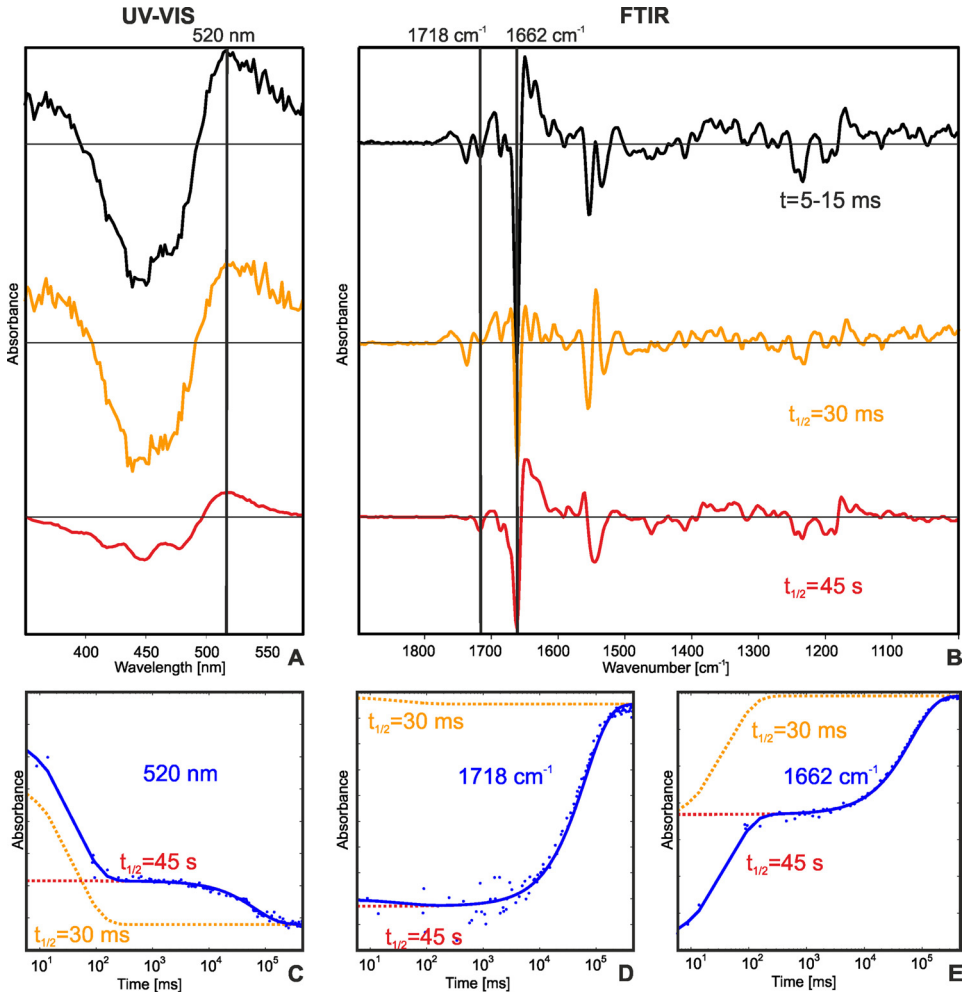

FIGURE 2. **Time-resolved absorbance changes in the WT protein induced by 20 ns laser excitation.** UV-visible (*A*) and FTIR (*B*) spectra are shown. The amplitude spectra (*orange* and *red*) were generated by a global fit of the complete combined dataset. In *A*: a P520-D470 difference spectrum (*black*) averaged over the first 10 ms is shown. The *red shift* of the absorption maximum indicates the accumulation of the P520 intermediate. In the corresponding IR difference spectrum, now assigned to the P520 intermediate, the deprotonation of Glu-90, indicated by the negative band at 1718 cm^{-1}, is observed. The first observed rate of 30 ms represents the P520 to P480 transition (*orange*). Here, the band shift of a carboxylic residue from 1728 to 1737 cm^{-1} is monitored. The slowest rate (*red*) of 45 s represents the P480 to D470 transition. The negative band at 1718 cm^{-1} indicates the reprotonation of Glu-90. Individual time-resolved absorbance changes at 520 nm in *C* and at 1718 cm^{-1} in *D* (Glu-90) are shown. The time-resolved data confirm that Glu-90 is already deprotonated in P520, being the putative open state. Whether deprotonation takes place in an earlier transition or simultaneously with the appearance of the P520 intermediate cannot be distinguished yet. Furthermore, the absorbance changes at 1662 cm^{-1} (*E*) show that the large structural changes (not time-resolved) of the protein backbone relax in two steps, in the P520 to P480 and the P480 to D470 transitions.

P520-D470 difference spectrum, as already assigned by Ritter *et al.* (7). The corresponding difference spectrum in the IR is shown in Fig. 2*B*. The amplitude spectrum of the 30-ms rate (orange) represents the P520 to P480 transition. The key features of the IR spectrum are a frequency shift of a not yet-assigned protonated glutamate or aspartate from 1728 to 1737 cm^{-1}, and a negative band at 1662 cm^{-1}, which was assigned to the amide-I mode of the protein backbone (7). The amplitude spectrum of the 45-s rate represents the transition from P480 to D470, in good agreement with the amplitude spectrum shown in Fig. 1.

Time-resolved absorbance changes at single wavelengths and wavenumbers, respectively, are shown in Fig. 2 (*C–E*). The absorbance change at 520 nm in Fig. 2*C* shows the instantaneous appearance (not time-resolved) of the P520 intermediate, followed by the transition from P520 to P480 in 30 ms and the transition from P480 to the D470 state in 45 s. The protonation changes of Glu-90 can followed at 1718 cm^{-1}, as assigned above (Fig. 2*D*). The deprotonation was not time-resolved, similar to the appearance of the P520 intermediate. Glu-90 then remained deprotonated in the P520 and P480 intermediates and was reprotonated during the relaxation to the D470 state in the last step. A conformational protein backbone change was observed at 1662 cm^{-1} (Fig. 2*E*). The appearance of the backbone change was not time-resolved, but we were able to assign the relaxation of this structural alteration to two steps, namely the P520 to P480 and the P480 to D470 transitions. Earlier studies in detergent suggested that the majority of structural changes occur during an early and the last step of the photocycle, whereas only minor structural alterations coincide with the decay of P520 (7, 9). Because the P520 intermediate is assumed to represent the open state, we propose that a protonation change of Glu-90, an environmental change at a not yet-assigned protonated carboxylic residue, and a large structural change of the protein backbone are key features of the opening/closing of the conductive pore.

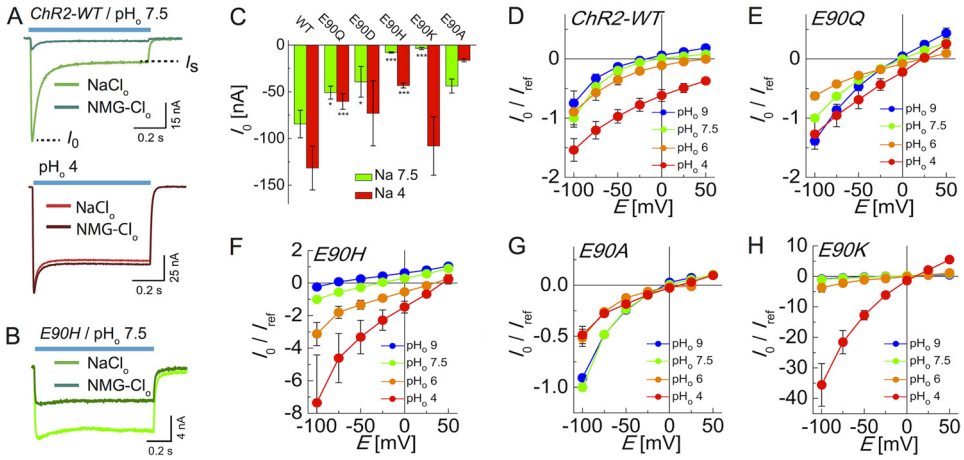

FIGURE 3. **Electrophysiological characterization of ChR2-WT and mutants of Glu-90.** Photocurrents of ChR2-WT (*A*) at pH$_o$ 7.5 and pH 4 and E90H (*B*) at pH$_o$ 7.5 in the absence and presence of 100 mM Na^+ at −100 mV (*blue bar*: 470 nm excitation). NMG-Cl was substituted by NaCl. *C*, averaged initial photocurrents (I_0) at pH$_o$ 7.5 and pH$_o$ 4 at −100 mV. Significance: $p < 0.05$ (*), $p < 0.005$ (***). Current-voltage relation of the initial current (I_0) at 100 mM Na^+ for wild-type ChR2 (*D*) and the mutants E90Q, E90A, E90H, and E90K (*E–H*). Measurements at pH$_o$ 7.5 and −100 mV were used as reference currents (I_{ref}); *error bars*: ±S.E.

Electrophysiological Measurements on WT ChR2 and Glu-90 Mutants—To confirm the proposal that Glu-90 functions as a gate and selectivity filter, we tested ChR2 activity in *Xenopus* oocytes after various substitutions at Glu-90 using two-electrode voltage clamp technology. Photocurrents were measured at pH 7.5 and 4 in the absence and presence of 100 mM Na^+. In the light, the initial current I_0 declined to a stationary level I_S, which was more obvious at neutral pH than at low pH (Fig. 3, *A* and *B*). At low pH, the current is carried by H^+ and only weakly influenced by Na^+, whereas at neutral pH the current is mainly carried by Na^+.

In the following discussion, we concentrate on the early current I_0 and do not further discuss I_S. Substitution of Glu-90 with Gln, Asp, His, Lys, and Ala in all cases reduced the photocurrent at pH 7.5 to different extents. This shows that the deprotonation of Glu-90, which is inhibited by the mutations, plays an important role in ion conductance at neutral conditions. At low pH this reduction was stronger for neutral residues E90Q and E90A and only minor for E90H and E90K suggesting that neutral residues at this place suppress proton conductance to a higher extent than the Na^+ conductance, whereas positive residues suppress Na^+ conductance more strongly. Moreover, the changes also depend on the membrane holding potential. To further evaluate the pH and voltage dependence, we plotted the I_0 values against voltage for four different pH values. All I/E plots were derived from measurements carried out at high Na^+ concentrations (100 mM). WT ChR2 showed moderate pH dependence of I_0 between pH 6 and 9 where the current was mainly carried by Na^+. The current increased at pH 4, but this increase is less obvious at low voltage where the displacement of Na^+ by H^+ is low (13). An identical pattern of dependence was seen in E90D (supplemental Fig. S1). In E90Q, which could not be deprotonated during the photocycle, the Na^+ currents, most clearly observed at pH 9, were like wild type; however, the addition of protons suppressed the currents until a slight recovery was seen at pH 4 (Fig. 3*E*). Similarly, E90A, originally introduced by Sugiyama *et al.*, shows no H^+ conductance, and the Na^+ conductance is inhibited at low pH (Fig. 3*G*) (11). In contrast, substitution of Glu-90 by the amphiphilic H almost totally suppressed Na^+ conductance (Fig. 3*B*), rendering the currents strongly pH-dependent over a wide pH range (Fig. 3*F*). In conclusion, specific substitutions at residue Glu-90 that result in conversion of the negative charge into neutral or positive might change both the conductance and selectivity of the channel, supporting our earlier claim that Glu-90 plays a pivotal role as a gate and selectivity filter of the conductive pore. All Glu-90 mutants showed differentially reduced conductance for H^+ and Na^+ in comparison with WT protein at pH 7.5 (Fig. 3*C*) and a variable competition between both ions, which is in line with our conclusion that a deprotonated Glu-90 is crucial for current size and ion selectivity. Quantitatively, the pH dependence of the I/E curves cannot be explained in detail yet, because the mutated protein might exhibit a different molecular activation mechanism as the WT protein, as is well known for *e.g.* bacteriorhodopsin (21, 22). For example, mutations of Glu-90 might shift the pK_a equilibrium of protonable groups within the protein differently, depending on their proton affinity and side chain size, which allows the placement of additional water molecules and thus alters the electrostatics within the protein.

Most bizarre is E90K, which has already been briefly described by Ruffert *et al.* (12). This mutant showed almost no conductance at pH range of 6 to 9 but a large current at pH 4 (Fig. 3*H*). At first glance this might appear to be a proton conductance; however, the reversal potential at pH 4 was unchanged, which clearly indicated the absence of a proton current. Na^+ and K^+ currents have also been excluded, and further studies are needed to identify the conducted ion. In summary, all mutations showed the importance of the deprotonation of Glu-90 for ion selectivity, although the gradual effect of the mutations on the conductance are not yet fully understood in detail.

Pore Formation in BR-based Homology Model—In the next step, we investigated whether the protonation change at Glu-90 revealed by FTIR spectroscopy influences the conformation of ChR2 in a manner comparable to the conformational changes seen in BR and other microbial rhodopsins due to protonation changes at crucial residues. Because there is no high resolution x-ray structure for ChR2 available yet, we created a dynamic

homology model of ChR2 based on the BR structure, using methods that we recently employed for the human olfactory receptor hOR2AG1 (25, 29). We are well aware that, although the overall 7-TM structures of ChR2 and BR are similar, both proteins might differ in structural details, such as the orientations of helices B, C, and D (4), and the exact position of their amino acid side chains. We nevertheless believe that the BR structure provides a sufficient template to investigate structural changes during the ChR2 photocycle. Sequence alignment of ChR2 and BR for the model construction was initiated with a multiple alignment of channelrhodopsins (ChR1, ChR2, VChR1, and VChR2), transporters (BR, HR (halorhodopsin), and XantoR (xantorhodopsin)), sensory rhodopsins (SR1, SR2, and ASR (*Anabaena* sensory rhodopsin)), and a blue-absorbing proteorhodopsin (supplemental Fig. S2). We then refined the alignment by application of criteria from dynamic homology modeling (29) by matching functionally relevant residues in BR with corresponding residues in ChR2 (Arg-82/Arg-120, Asp-85/Glu-123, Asp-96/His-134, Asp-115/Asp-156, Asp-212/Asp-253, and Lys-216/Lys-257).

Due to the poor overall homology of the channelrhodopsins with other microbial rhodopsins, we had to incorporate information from spectroscopic as well as electrophysiological experiments into the model. In particular, different sequence alignments for helix B of ChR2 and BR have been suggested in former studies (1, 2, 4, 41). These alignments differ mostly in positioning an intriguing glutamate cluster within the ChR2 sequence that consists of five glutamates, namely Glu-82, Glu-83, Glu-90, Glu-97, and Glu-101. Three of these glutamates, Glu-82, Glu-90, and Glu-101, are conserved in all known ChRs (42). Detailed information on the various alignments regarding the glutamate cluster suggested by different groups can be found in the supplemental materials.

We built the homology model of ChR2 with the whole glutamate cluster located within helix B (supplemental Fig. S3*D*). The results of our simulations favored an arrangement with this glutamate cluster oriented toward the inside of the protein (more information on protein modeling can be found in the supplemental materials). This arrangement of the glutamate cluster has been previously suggested (12) and is supported by earlier electrophysiological experiments. Replacement of Glu-90, Glu-97, and Glu-101 in ChR2 by positively charged or nonpolar residues leads to modulation of the ion selectivity and conductance of ChR2 (11–13). Therefore it is proposed that Glu-90, Glu-97, and Glu-101 line the ChR2 conductive pore within (11, 12). Substitution of Glu-101 with alanine additionally results in significantly altered gating kinetics (11).

Because our FTIR spectroscopic results reveal deprotonation of Glu-90 during the ChR2 photocycle, we simulated this deprotonation and analyzed the resulting influx of water molecules. The change in protein-bound water distribution should provide insight into possible pore formation within the helical bundle. We are well aware that, because of the putative differences between the overall structures of BR and ChR2, the resulting pore in our ChR2 model might differ in some details, but we are convinced that our homology model reproduces the location of the pore at lower resolution. We started with protonated Glu-90, then deprotonated Glu-90 after 20 ns of MD simulation and ran the simulation for another 100 ns. Changes in protein-bound water molecules are determined by the distribution of water molecules ("water densities") within the protein during the MD simulation (43). We searched for different water penetration depths, which might indicate channel opening. The results are shown in Fig. 4. When Glu-90 was protonated, water molecules invaded from the extracellular side up to the retinal, whereas only a small invasion was observed from the intracellular side. The environment of protonated Glu-90 seems to be hydrophobic enough to repel water molecules. This discontinuous water distribution throughout ChR2 prevented the transfer of hydrated ions and seemed to represent the nonconductive closed state of ChR2. When Glu-90 was deprotonated, it became solvated (Fig. 4) in our homology model. The intracellular side then started to fill up with water molecules and, thereby, became more hydrophilic. This might indicate the formation of a continuous aqueous pore through the whole protein (Fig. 4). Nevertheless, gaps remained between the densities. Müller *et al.* (4) demonstrated using electron microscopy that helix C in the ChR2 dimer is positioned more toward the outer face of the helical bundle in comparison to BR; this positioning would result in a larger intramolecular space for intruding water. However, our simulations suggest that the deprotonation of Glu-90, as experimentally observed in FTIR experiments, induces the formation of a protein-bound water network spanning the whole protein. This seems to represent the first steps toward pore formation during the photocycle of ChR2.

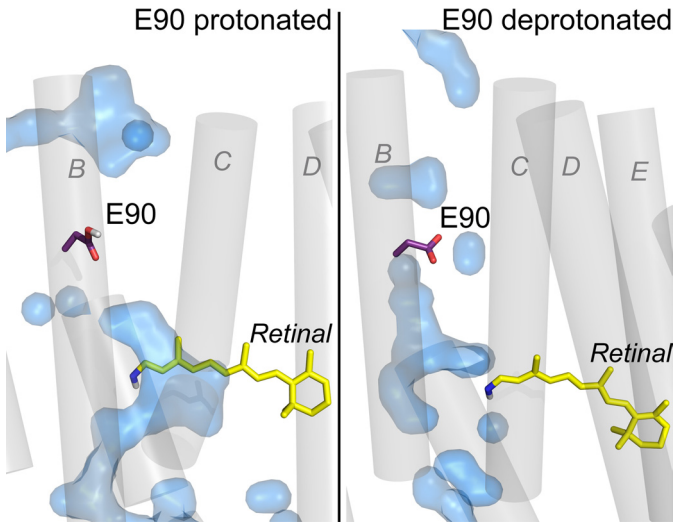

FIGURE 4. **Water densities (43) reflecting the protein-internal volume in the ChR2 homology model occupied by water molecules during MD simulations depending on the protonation state of Glu-90.** Water density distribution changes within ChR2 due to deprotonation of Glu-90. When Glu-90 is protonated (*left panel*), two distinct regions of intruding water molecules are observed, with Glu-90 being found in the middle of the barrier between them. When Glu-90 is deprotonated (*right panel*), the water influx is altered. The former unsolvated region around Glu-90 starts to fill up with water. The extracellular side is still more solvated than the intracellular side of the protein. The alteration of water densities results in an almost continuously spanning water-filled pore.

DISCUSSION

Based on the MD simulations, which revealed significant water influx into the protein upon deprotonation of Glu-90, we

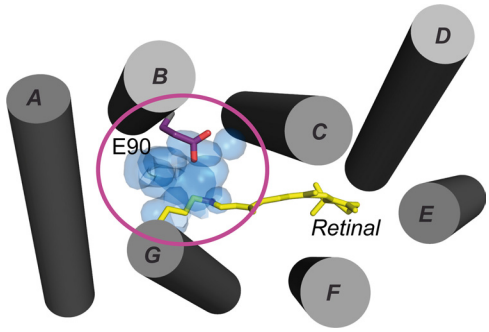

FIGURE 5. **Putative location of the conductive pore within the helical bundle of the BR-based ChR2 homology model (intracellular view).** ChR2 is shown in *gray*, the chromophore retinal is highlighted in *yellow*, Glu-90 is in *purple*, and penetrating water molecules are shown as *blue surfaces*. MD simulation reveals that the location of the conductive pore within the helical bundle of ChR2 is between helices A, B, C, and G, in direct contact with the chromophore and the RSB, indicated by the *red circle*. MD simulations reveal Glu-90 to be flanking the conductive pore.

hypothesize the conductive pore within ChR2 to be located between helices A, B, C, and G as shown in Fig. 5. As mentioned above, we believe that, due to the different placement of helix C in ChR2 with respect to BR, the actual pore in ChR2 will be larger than the one observed in our model.

In conclusion, results from FTIR spectroscopy, electrophysiological studies, and MD simulations lead to the following proposed molecular mechanism of ChR2. Upon illumination of ChR2, structural rearrangements that correlate with the reprotonation of the retinal Schiff base might lead to the deprotonation of Glu-90 and to a transition of the intracellular half of the protein from a hydrophobic to a hydrophilic environment. A subsequent influx of water molecules from intra- and extracellular protein surfaces might constitute the ion channel pore, which is mainly spanned by glutamates in Helix B.

The pore appears to be embedded between helices A, B, C, and G. Modification of Glu-90 severely alters the selectivity of the channel but does not significantly change the gating kinetics. This observation suggests that Glu-90 functions as a gate and selectivity filter of the conducting pore. Structural changes that include the deprotonation of Glu-90 in WT ChR2 open the gate by effecting the formation of the conducting pore, the selectivity of which can be altered by Glu-90 substitution.

Throughout the microbial-type rhodopsin family, the third (C) to seventh (G) transmembrane helices are believed to form a general retinal binding and interaction motif. We therefore assume that structures and residues essential for the ion conductance of ChR2 are located within helices A and B. In particular, helix B exhibits enhanced hydrophilicity in ChR family members, a feature that is not seen in proton pumps or sensory rhodopsins but is believed to be necessary for ion transport. This assumption is in good agreement with the experimental observation that the three glutamates, Glu-90, Glu-97, and Glu-101, within helix B are crucial for the ChR2 conductance. According to our results, we assume the ChR2 monomer to be the functional unit. In terms of optogenetic engineering, our dynamic homology model provides insights into the dynamics of formation of the ion pore.

The proposed dynamic homology model of ChR2 incorporates results from time-resolved spectroscopic and electrophysiological experiments. It therefore provides essential features of the molecular mechanism of ChR2 and might serve as a dynamic framework for the interpretation of a static high-resolution x-ray structure, which is not yet available. In any case, such an x-ray structural model will not provide information on the protonation state of Glu-90 or its deprotonation, or the influence of the deprotonation during the photocycle on the ion conductance. Thus, the proposed dynamic model emerging from time-resolved spectroscopic and electrophysiological experiments will in any case provide essential features of the molecular mechanism of ChR-2. The proposed mechanism will help to optimize ion selectivity of ChR2 to generate more powerful optogenetic tools.

Acknowledgments—We thank Anja Koch and Roman Kazmin for excellent technical assistance with preparing ChR2 mutants and Katja Stehfest for discussion during the early phase of this project. Calculations were performed on the Max-Planck Partner Institute for Computational Biology Shanghai High Performance Computing cluster.

REFERENCES

1. Sineshchekov, O. A., Jung, K. H., and Spudich, J. L. (2002) Two rhodopsins mediate phototaxis to low- and high-intensity light in *Chlamydomonas reinhardtii*. *Proc. Natl. Acad. Sci. U.S.A.* **99,** 8689–8694
2. Nagel, G., Szellas, T., Huhn, W., Kateriya, S., Adeishvili, N., Berthold, P., Ollig, D., Hegemann, P., and Bamberg, E. (2003) Channelrhodopsin-2, a directly light-gated cation-selective membrane channel. *Proc. Natl. Acad. Sci. U.S.A.* **100,** 13940–13945
3. Yizhar, O., Fenno, L. E., Davidson, T. J., Mogri, M., and Deisseroth, K. (2011) Optogenetics in neural systems. *Neuron* **71,** 9–34
4. Müller, M., Bamann, C., Bamberg, E., and Kühlbrandt, W. (2011) Projection structure of channelrhodopsin-2 at 6 Å resolution by electron crystallography. *J. Mol. Biol.* **414,** 86–95
5. Verhoefen, M. K., Bamann, C., Blöcher, R., Förster, U., Bamberg, E., and Wachtveitl, J. (2010) The photocycle of channelrhodopsin-2. Ultrafast reaction dynamics and subsequent reaction steps. *Chemphyschem* **11,** 3113–3122
6. Ernst, O. P., Sánchez Murcia, P. A., Daldrop, P., Tsunoda, S. P., Kateriya, S., and Hegemann, P. (2008) Photoactivation of channelrhodopsin. *J. Biol. Chem.* **283,** 1637–1643
7. Ritter, E., Stehfest, K., Berndt, A., Hegemann, P., and Bartl, F. J. (2008) Monitoring light-induced structural changes of Channelrhodopsin-2 by UV-visible and Fourier transform infrared spectroscopy. *J. Biol. Chem.* **283,** 35033–35041
8. Bamann, C., Gueta, R., Kleinlogel, S., Nagel, G., and Bamberg, E. (2010) Structural guidance of the photocycle of channelrhodopsin-2 by an interhelical hydrogen bond. *Biochemistry* **49,** 267–278
9. Radu, I., Bamann, C., Nack, M., Nagel, G., Bamberg, E., and Heberle, J. (2009) Conformational changes of channelrhodopsin-2. *J. Am. Chem. Soc.* **131,** 7313–7319
10. Lanyi, J. K. (2006) Proton transfers in the bacteriorhodopsin photocycle. *Biochim. Biophys. Acta* **1757,** 1012–1018
11. Sugiyama, Y., Wang, H., Hikima, T., Sato, M., Kuroda, J., Takahashi, T., Ishizuka, T., and Yawo, H. (2009) Photocurrent attenuation by a single polar-to-nonpolar point mutation of channelrhodopsin-2. *Photochem. Photobiol. Sci.* **8,** 328–336
12. Ruffert, K., Himmel, B., Lall, D., Bamann, C., Bamberg, E., Betz, H., and Eulenburg, V. (2011) Glutamate residue 90 in the predicted transmembrane domain 2 is crucial for cation flux through channelrhodopsin 2. *Biochem. Biophys. Res. Commun.* **410,** 737–743
13. Gradmann, D., Berndt, A., Schneider, F., and Hegemann, P. (2011) Rectification of the channelrhodopsin early conductance. *Biophys. J.* **101,** 1057–1068

14. Lin, J. Y., Lin, M. Z., Steinbach, P., and Tsien, R. Y. (2009) Characterization of engineered channelrhodopsin variants with improved properties and kinetics. *Biophys. J.* **96,** 1803–1814
15. Gunaydin, L. A., Yizhar, O., Berndt, A., Sohal, V. S., Deisseroth, K., and Hegemann, P. (2010) Ultrafast optogenetic control. *Nat. Neurosci.* **13,** 387–392
16. Stehfest, K., and Hegemann, P. (2010) Evolution of the channelrhodopsin photocycle model. *Chemphyschem* **11,** 1120–1126
17. Berndt, A., Schoenenberger, P., Mattis, J., Tye, K. M., Deisseroth, K., Hegemann, P., and Oertner, T. G. (2011) High-efficiency channelrhodopsins for fast neuronal stimulation at low light levels. *Proc. Natl. Acad. Sci. U.S.A.* **108,** 7595–7600
18. Joh, N. H., Min, A., Faham, S., Whitelegge, J. P., Yang, D., Woods, V. L., and Bowie, J. U. (2008) Modest stabilization by most hydrogen-bonded side-chain interactions in membrane proteins. *Nature* **453,** 1266–1270
19. Berndt, A., Yizhar, O., Gunaydin, L. A., Hegemann, P., and Deisseroth, K. (2009) Bi-stable neural state switches. *Nat. Neurosci.* **12,** 229–234
20. Schoenenberger, P., Gerosa, D., and Oertner, T. G. (2009) Temporal control of immediate early gene induction by light. *PLoS One* **4,** e8185
21. Wolf, S., Freier, E., Potschies, M., Hofmann, E., and Gerwert, K. (2010) Directional proton transfer in membrane proteins achieved through protonated protein-bound water molecules. A proton diode. *Angew. Chem. Int. Ed. Engl.* **49,** 6889–6893
22. Freier, E., Wolf, S., and Gerwert, K. (2010) Proton transfer via a transient linear water-molecule chain in a membrane protein. *Proc. Natl. Acad. Sci. U.S.A.* **108,** 11435–11439
23. Doszczak, L., Kraft, P., Weber, H. P., Bertermann, R., Triller, A., Hatt, H., and Tacke, R. (2007) Prediction of perception. Probing the hOR17–4 olfactory receptor model with silicon analogues of bourgeonal and lilial. *Angew. Chem. Int. Ed. Engl.* **46,** 3367–3371
24. Kufareva, I., Rueda, M., Katritch, V., Stevens, R. C., and Abagyan, R. (2011) Status of GPCR modeling and docking as reflected by community-wide GPCR Dock 2010 assessment. *Structure* **19,** 1108–1126
25. Gelis, L., Wolf, S., Hatt, H., Neuhaus, E. M., and Gerwert, K. (2011) Prediction of a ligand-binding niche within a human olfactory receptor by combining site-directed mutagenesis with dynamic homology modeling. *Angew. Chem. Int. Ed. Engl.* doi: 10.1002/ anie.201107509
26. Garczarek, F., and Gerwert, K. (2006) Functional waters in intraprotein proton transfer monitored by FTIR difference spectroscopy. *Nature* **439,** 109–112
27. Gerwert, K., Hess, B., Soppa, J., and Oesterhelt, D. (1989) Role of aspartate-96 in proton translocation by bacteriorhodopsin. *Proc. Natl. Acad. Sci. U.S.A.* **86,** 4943–4947
28. Gerwert, K., Souvignier, G., and Hess, B. (1990) Simultaneous monitoring of light-induced changes in protein side-group protonation, chromophore isomerization, and backbone motion of bacteriorhodopsin by time-resolved Fourier-transform infrared spectroscopy. *Proc. Natl. Acad. Sci. U.S.A.* **87,** 9774–9778
29. Wolf, S., Böckmann, M., Höweler, U., Schlitter, J., and Gerwert, K. (2008) Simulations of a G protein-coupled receptor homology model predict dynamic features and a ligand binding site. *FEBS Lett.* **582,** 3335–3342
30. Belrhali, H., Nollert, P., Royant, A., Menzel, C., Rosenbusch, J. P., Landau, E. M., and Pebay-Peyroula, E. (1999) Protein, lipid and water organization in bacteriorhodopsin crystals. A molecular view of the purple membrane at 1.9 A resolution. *Structure* **7,** 909–917
31. Schneider, M., Wolf, S., Schlitter, J., and Gerwert, K. (2011) The structure of active opsin as a basis for identification of GPCR agonists by dynamic homology modelling and virtual screening assays. *FEBS Lett.* **585,** 3587–3592
32. Stehfest, K., Ritter, E., Berndt, A., Bartl, F., and Hegemann, P. (2010) The branched photocycle of the slow-cycling channelrhodopsin-2 mutant C128T. *J. Mol. Biol.* **398,** 690–702
33. Molday, R. S., and MacKenzie, D. (1983) Monoclonal antibodies to rhodopsin. Characterization, cross-reactivity, and application as structural probes. *Biochemistry* **22,** 653–660
34. Marin, E. P., Krishna, A. G., Zvyaga, T. A., Isele, J., Siebert, F., and Sakmar, T. P. (2000) The amino terminus of the fourth cytoplasmic loop of rhodopsin modulates rhodopsin-transducin interaction. *J. Biol. Chem.* **275,** 1930–1936
35. Ernst, O. P., Meyer, C. K., Marin, E. P., Henklein, P., Fu, W. Y., Sakmar, T. P., and Hofmann, K. P. (2000) Mutation of the fourth cytoplasmic loop of rhodopsin affects binding of transducin and peptides derived from the carboxyl-terminal sequences of transducin α and γ subunits. *J. Biol. Chem.* **275,** 1937–1943
36. Fritze, O., Filipek, S., Kuksa, V., Palczewski, K., Hofmann, K. P., and Ernst, O. P. (2003) Role of the conserved NPxxY(x)5,6F motif in the rhodopsin ground state and during activation. *Proc. Natl. Acad. Sci. U.S.A.* **100,** 2290–2295
37. Canutescu, A. A., Shelenkov, A. A., and Dunbrack, R. L., Jr. (2003) A graph-theory algorithm for rapid protein side-chain prediction. *Protein Sci.* **12,** 2001–2014
38. Hoeweler, U. (2007) MAXIMOBY 8.1 and MOBY 3.0. CHEOPS Molecular Modelling, Altenberge, Germany
39. Tieleman, D. P., Forrest, L. R., Sansom, M. S., and Berendsen, H. J. (1998) Lipid properties and the orientation of aromatic residues in OmpF, influenza M2, and alamethicin systems. Molecular dynamics simulations. *Biochemistry* **37,** 17554–17561
40. Hess, B., Kutzner, C., van der Spoel, D., and Lindahl, E. (2008) GROMACS 4: algorithms for highly efficient, load-balanced, and scalable molecular simulation. *J. Chem. Theory Comput.* **4,** 435–447
41. Suzuki, T., Yamasaki, K., Fujita, S., Oda, K., Iseki, M., Yoshida, K., Watanabe, M., Daiyasu, H., Toh, H., Asamizu, E., Tabata, S., Miura, K., Fukuzawa, H., Nakamura, S., and Takahashi, T. (2003) Archaeal-type rhodopsins in *Chlamydomonas*. Model structure and intracellular localization. *Biochem. Biophys. Res. Commun.* **301,** 711–717
42. Govorunova, E. G., Spudich, E. N., Lane, C. E., Sineshchekov, O. A., and Spudich, J. L. (2011) New channelrhodopsin with a red-shifted spectrum and rapid kinetics from *Mesostigma viride*. *MBio* **2,** e00115–00111
43. Kandt, C., Schlitter, J., and Gerwert, K. (2004) Dynamics of water molecules in the bacteriorhodopsin trimer in explicit lipid/water environment. *Biophys. J.* **86,** 705–717